Magnetic structures and magnetoelastic coupling of Fe-doped hexagonal manganites $LuMn_{1-x}Fe_xO_3(0 \leqslant x \leqslant 0.3)$

Zhendong Fu,[1,*] Harikrishnan S. Nair,[2] Yinguo Xiao,[3,†] Anatoliy Senyshyn,[4,5] Vladimir Y. Pomjakushin,[6] Erxi Feng,[1] Yixi Su,[1] W. T. Jin,[1] and Thomas Brückel[3]

[1]*Jülich Centre for Neutron Science (JCNS) at Heinz Maier-Leibnitz Zentrum (MLZ), Forschungszentrum Jülich GmbH, Lichtenbergstraße 1, D-85748 Garching, Germany*

[2]*Highly Correlated Matter Research Group, Physics Department, University of Johannesburg, P.O. Box 524, Auckland Park 2006, South Africa*

[3]*Jülich Centre for Neutron Science (JCNS) and Peter Grünberg Institut (PGI), Jülich Aachen Research Alliance-Fundamentals of Future Information Technology (JARA-FIT), Forschungszentrum Jülich GmbH, D-52425 Jülich, Germany*

[4]*Institute for Material Science, Darmstadt University of Technology, D-64287 Darmstadt, Germany*

[5]*Forschungsneutronenquelle Heinz-Maier Leibnitz, Technische Universität München, Licthenbergstraße 1, D-85747 Garching, Germany*

[6]*Laboratory for Neutron Scattering and Imaging, Paul Scherrer Institut (PSI), 5232 Villigen PSI, Switzerland*

(Received 9 March 2016; revised manuscript received 18 July 2016; published 30 September 2016)

We have studied the crystal and magnetic structures of Fe-doped hexagonal manganites $LuMn_{1-x}Fe_xO_3$ (x = 0,0.1,0.2, and 0.3) by using bulk magnetization and neutron powder diffraction methods. The samples crystalize consistently in a hexagonal structure and maintain the space group $P6_3cm$ from 2 to 300 K. The Néel temperature T_N increases continuously with increasing Fe doping. In contrast to a single Γ_4 representation in $LuMnO_3$, the magnetic ground state of the Fe-doped samples can only be described with a combination of $\Gamma_3(P6_3'cm')$ and $\Gamma_4(P6_3'c'm)$ irreducible representations, whose contributions have been quantitatively estimated. The drastic effect of Fe doping is highlighted by composition-dependent spin reorientations. A phase diagram of the entire composition series is proposed based on the present result and those reported in literature. Our result demonstrates the importance of tailoring compositions in increasing magnetic transition temperatures of multiferroic systems.

DOI: 10.1103/PhysRevB.94.125150

I. INTRODUCTION

Multiferroics are materials in which both ferroelectric and magnetic transitions can occur and where both ordering phenomena coexist in a single phase [1]. The possible coupling between magnetism and ferroelectricity in multiferroics has drawn extensive attention because of the potential technological significance in controlling one order parameter through the other. The hexagonal (h) manganites $RMnO_3$(R = rare earth) are an interesting group of multiferroics that exhibit a rich variety of physical phenomena [2,3]. Although the ferroelectric transition temperature ($T_F \sim 1000$ K) of h-$RMnO_3$ is much higher than its antiferromagnetic (AFM) transition temperature ($T_N \sim 100$ K) [3], evidence for coupling between magnetic and electric dipole moments has been revealed by means of dielectric constant measurements and high-resolution neutron diffraction [4,5].

In the ferroelectric state, h-$RMnO_3$ manganites are crystallized in the hexagonal structure with the space group $P6_3cm$ [6]. As shown in Fig. 1(a), each Mn atom and its five adjacent oxygen atoms form a MnO_5 bipyramid, where two oxygen atoms are at the apexes and three oxygen atoms are in the equatorial plane of the MnO_5 bipyramid. The corner-sharing MnO_5 bipyramids form a triangular lattice in the ab plane of the hexagonal structure and are well separated from each other along the c axis by the plane of R ions. Pronounced magnetic frustration has been observed in h-$RMnO_3$, arising from the 120° triangular lattice of antiferromagnetically coupled Mn^{3+} ions [7]. The Mn-O-O-Mn superexchange interaction between adjacent triangular planes ($z = 0$ and $z = 1/2$) is found much weaker than the in-plane Mn-O-Mn superexchange interaction [3,8].

The Mn^{3+} moments in h-$RMnO_3$ order below T_N in a noncollinear spin structure with a 120° angular difference between neighboring spins in the ab plane [4,5]. However, precise determination of the magnetic structure of h-$RMnO_3$ is often nontrivial due to the existence of homometric spin configurations and limited instrumental resolution. For example, as one of the most intensively studied h-$RMnO_3$, $YMnO_3$ has an AFM structure with $k = 0$ vector below T_N, as suggested by neutron diffraction measurements. According to the theoretical analysis using magnetic group theory, altogether six magnetic structures are found to be possible: four one-dimensional (1D; Γ_1,Γ_2,Γ_3, and Γ_4) and two two-dimensional (2D; Γ_5 and Γ_6) irreducible representations [9]. The four 1D models are shown in Figs. 1(b)–1(e); $\Gamma_1(P6_3cm)$ and $\Gamma_2(P6_3c'm')$ have antiparallel coupling between $z = 0$ and $z = 1/2$ moments, while $\Gamma_3(P6_3'cm')$ and $\Gamma_4(P6_3'c'm)$ have parallel coupling. The moment on the [100] axis is perpendicular to the [100] axis in Γ_1 and Γ_4 and parallel in Γ_2 and Γ_3. Earlier neutron powder diffraction (NPD) studies have proposed that the magnetic structure of $YMnO_3$ is either Γ_1 or Γ_3, which were indistinguishable within the experimental resolution [10,11]. The second harmonic generation results agree better with the Γ_3 magnetic symmetry [12,13], while Γ_1 is also favored in other literature [14,15]. The later polarimetric neutron study has suggested a $\Gamma_6(P6_3')$ magnetic symmetry with Mn moments inclined at 11° with respect to Γ_3 [16].

*z.fu@fz-juelich.de
†y.xiao@fz-juelich.de

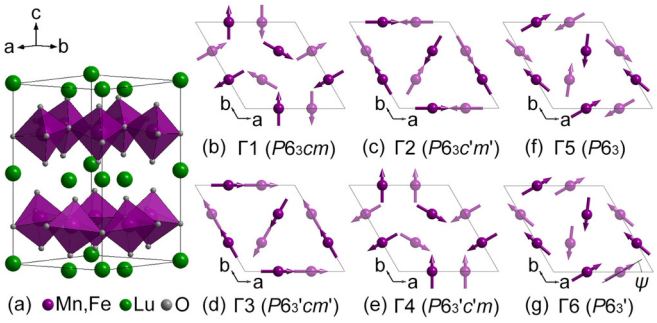

FIG. 1. (a) Schematic of the crystal structure of $LuMn_{1-x}Fe_xO_3$; (b)–(g) 1D and 2D magnetic representations of $LuMn_{1-x}Fe_xO_3$: $\Gamma_1(P6_3cm)$, $\Gamma_2(P6_3c'm')$, $\Gamma_3(P6_3'cm')$, $\Gamma_4(P6_3'c'm)$, $\Gamma_5(P6_3)$, and $\Gamma_6(P6_3')$. The lighter and darker symbols denote Mn/Fe atoms displaced along c by 1/2 of the unit cell.

The key parameter in selecting a given magnetic structure or the occurrence of a spin reorientation transition in hexagonal manganites has been attributed to the position x of Mn ions within the triangular plane with reference to a critical threshold of 1/3 using high-resolution NPD and inelastic neutron scattering methods [17,18].

Despite the similarities in physical properties with $YMnO_3$, $LuMnO_3$ in AFM phase has been described by either a Γ_4 representation [12,19,20] or a Γ_2 representation [21]. Doping Lu at Y site of $YMnO_3$ introduces a continuous variation in magnetic structure from the Γ_3 to Γ_4 representation, which can be explained in terms of the chemical pressure effects due to doping [19]. It is also interesting to explore the effect of the magnetic doping at the Mn site on the magnetic structure. A single phase of h-$YMn_{1-x}Fe_xO_3$ has been obtained for $x \leqslant 0.3$ [22]. The 10% Fe doping at the Mn site of $YMnO_3$ results in a decrease of T_N from 75 to 60 K and a spin reorientation transition from Γ_3 to $\Gamma_3 + \Gamma_4$ at $T_{SR} \sim 35$ K [23]. In a recent NPD study of Fe-doped (up to 10%) h-$YMn_{1-x}Fe_xO_3$, the magnetic ground state has been found to change from a highly frustrated (Γ_1 in $YMnO_3$) to a lowly frustrated (Γ_2 in $YMn_{0.9}Fe_{0.1}O_3$) magnetic structure via a mixed [$(\Gamma_1 + \Gamma_2)$ in $YMn_{0.95}Fe_{0.05}O_3$] configuration [15]. The Fe doping in $LuMnO_3$ has also attracted attention due to the improved magnetic properties of h-$LuFeO_3$ as compared with those of h-$LuMnO_3$. A single phase of solid solution has been achieved in the half doped $LuMn_{0.5}Fe_{0.5}O_3$ [2,24]. Indeed the T_N (~110 K) of $LuMn_{0.5}Fe_{0.5}O_3$ is higher than that of $LuMnO_3$ by about 20 K. The magnetic ground state of $LuMn_{0.5}Fe_{0.5}O_3$ has been described by a single magnetic representation Γ_1 or Γ_3 [2,24]. The crystal and magnetic structures of the Fe-rich compounds, $LuMn_{1-x}Fe_xO_3$ ($x \geqslant 0.5$), have been investigated using powder diffraction and inelastic neutron scattering in Ref. [24], which will be revisited later in the discussion. In the present paper, we report the effect of Fe doping (up to 30%) on the magnetic structure and magnetic properties of h-$LuMnO_3$.

II. EXPERIMENTAL DETAILS

The polycrystalline samples were synthesized by the standard solid-state reaction method [2,25]. Subsequent x-ray diffraction (XRD) was done on a Huber x-ray diffractometer (Huber G670) with Cu-Kα radiation from 20 to 300 K. The XRD patterns (see Fig. S1 of the Supplemental Material [26]) for all as-prepared samples indicate no trace of impurity phases. Magnetization data were taken using a Quantum Design Dynacool Physical Property Measurement System. The temperature-dependent NPD experiments were carried out on the high-resolution powder diffractometer for thermal neutrons (HRPT) [27] at the Swiss Spallation Neutron Source (SINQ) of the Paul Scherrer Institute (PSI; Villigen, Switzerland), and on the high-resolution powder diffractometer SPODI [28] at the Heinz Maier-Leibnitz Zentrum (MLZ), Garching, Germany. During measurement, HRPT was running in high-intensity mode with the wavelength $\lambda = 1.886$ Å. The wavelength used on SPODI was 1.5483 Å. The NPD data are normalized by the spectrum of a vanadium standard. The irreducible representations for magnetic structure were obtained using SARAh package [29]. The nuclear and magnetic structure refinements were performed using Rietveld method [30] with FULLPROF suite [31].

III. RESULTS AND ANALYSIS

As shown in Fig. 2(a), the temperature dependences of molar magnetization M of $LuMn_{1-x}Fe_xO_3$ ($x = 0,0.1,0.2$, and 0.3) were measured under an external field of 1 T from 5 to 310 K. All four samples show a magnetic phase transition in the range between 90 and 115 K, corresponding to the Néel transition T_N from the paramagnetic state to the long-range ordered AFM state. Considering also the recently published paper on $LuMn_{0.5}Fe_{0.5}O_3$ [2], we find that the T_N of $LuMn_{1-x}Fe_xO_3$ increases from 92 to 112 K when the Fe-doping ratio increases

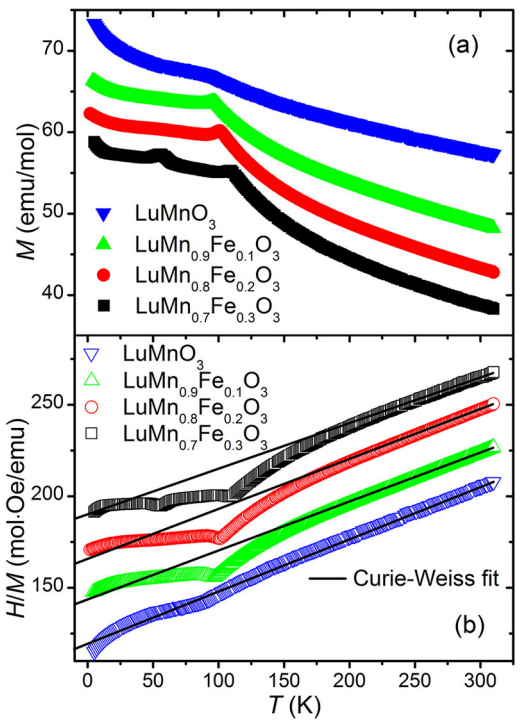

FIG. 2. (a) Molar magnetization for $LuMn_{1-x}Fe_xO_3$($x = 0,0.1$, 0.2, and 0.3) as a function of temperature between 5 and 310 K; (b) temperature dependence of the inverse susceptibility with the fit using Curie-Weiss law. The curves are shifted vertically for clarity.

TABLE I. The Curie-Weiss temperature θ_{CW}, the Néel temperature T_N, the frustration parameter f, the temperature of spin reorientation T_{SR}, and the effective paramagnetic moment μ_{eff} of $LuMn_{1-x}Fe_xO_3 (x \leqslant 0.5)$. The values for $LuMn_{0.5}Fe_{0.5}O_3$ are taken from Ref. [2].

	$LuMnO_3$	$LuMn_{0.9}Fe_{0.1}O_3$	$LuMn_{0.8}Fe_{0.2}O_3$	$LuMn_{0.7}Fe_{0.3}O_3$	$LuMn_{0.5}Fe_{0.5}O_3$
$\lvert\vartheta_{CW}\rvert$ (K)	776(3)	542(7)	510(4)	552(6)	946
T_N(K)	92(1)	102(1)	105(1)	109(1)	112
f	8.4(2)	5.3(1)	4.8(1)	5.1(1)	8.5
T_{SR}(K)	–	–	–	55(1)	55
$\mu_{eff}(\mu_B)$	4.88(5)	5.17(6)	5.15(5)	5.27(4)	5.41(4)

from 0 to 0.5. Similar to $LuMn_{0.5}Fe_{0.5}O_3$, $LuMn_{0.7}Fe_{0.3}O_3$ exhibits another phase transition below T_N at $T_{SR} \sim 55$ K. We tentatively attribute it to a spin reorientation transition, which will be discussed later in this paper. The inverse susceptibility H/M *vs* temperature T curves are plotted in Fig. 2(b). The fit with the Curie-Weiss law to the data above 250 K reveals a negative Curie-Weiss temperature ϑ_{CW} in all samples, indicative of predominant AFM coupling among magnetic moments. The effective paramagnetic moment μ_{eff} of each sample is calculated from the Curie constant and listed in Table I. The values of the frustration parameter, $f = |\vartheta_{CW}|/T_N$, for the samples are around or larger than five, suggesting that magnetic frustration may exist in the samples. The triangular-lattice arrangement of the Mn atoms has been considered as the main source for the geometrical magnetic frustration in h-$RMnO_3$ [2,14,16,19,32]. However, we should point out that the difference between ϑ_{CW} and T_N can also be due to the low dimensionality of the magnetic lattice because the intraplane coupling is much stronger than the interplane coupling. The deviation from Curie-Weiss behavior in the samples takes place at temperatures higher than T_N due to the onset of magnetic 2D short-range correlations, as evidenced by the magnetic diffuse scattering, which will be discussed later. The obtained T_N, T_{SR}, ϑ_{CW}, and μ_{eff} are summarized in Table I. The field dependence of magnetization has been taken from all samples at 5 K. The absence of hysteresis rules out a ferromagnetic contribution to the magnetic susceptibility.

To investigate the Fe-doping effect on the crystal and magnetic structures of $LuMnO_3$, the NPD patterns for $LuMn_{1-x}Fe_xO_3$ ($x = 0, 0.1$, and 0.3) were recorded from 2 to 300 K on HRPT, and those for $x = 0.2$ were recorded from 5 to 300 K on SPODI. Representative NPD patterns measured at 5 and 300 K on each sample are shown in Fig. 3 as a function of $Q(\equiv 4\pi\sin(\vartheta)/\lambda)$. A combined XRD and NPD refinement using FULLPROF was performed for the data collected above 20 K. The result of the Rietveld refinement of the XRD data is shown in Fig. S1 of the Supplemental Material [26]. It is further confirmed from the well-refined diffraction patterns that our samples are of single phase with little trace of impurities. In the temperature range of interest from 5 to 300 K, no symmetry change has been observed, and the nuclear structure of all samples belongs to the space group $P6_3cm$.

All four samples show clear magnetic reflections below T_N. Figure 4 shows the low-angle part of the NPD patterns recorded at 5 K. For comparison, the data of $LuMn_{0.5}Fe_{0.5}O_3$ from our previous publication is also shown [2]. It is obvious that Fe doping at the Mn-site has a dramatic influence on the magnetic structure of h-$LuMnO_3$. The

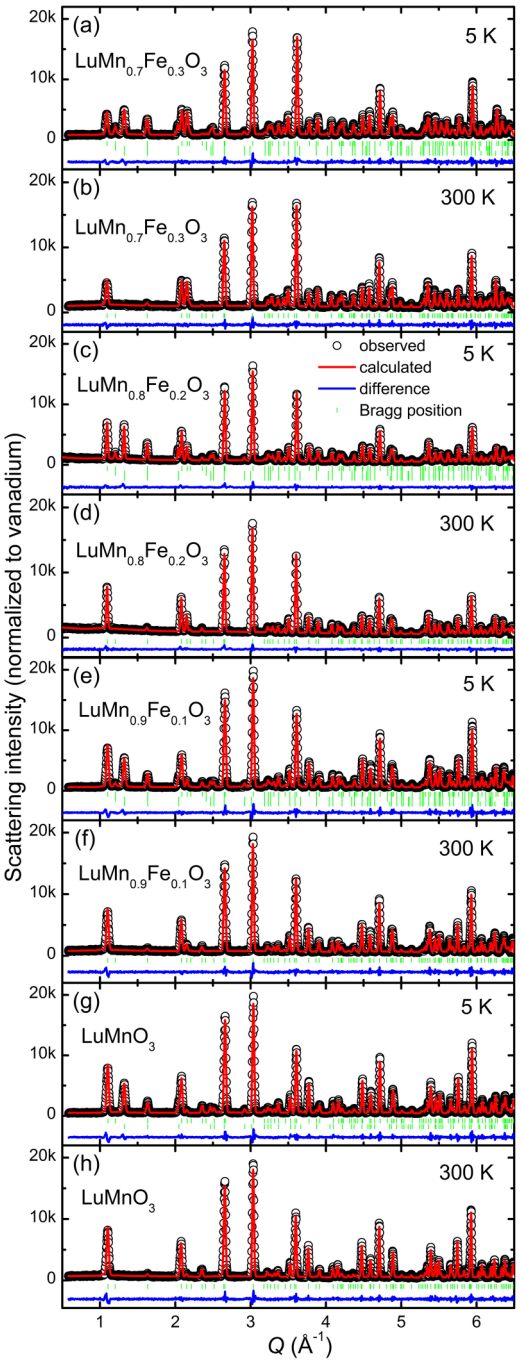

FIG. 3. The NPD patterns for $LuMn_{1-x}Fe_xO_3 (x = 0, 0.1, 0.2$, and 0.3) measured at 5 and 300 K, along with Rietveld refinement results.

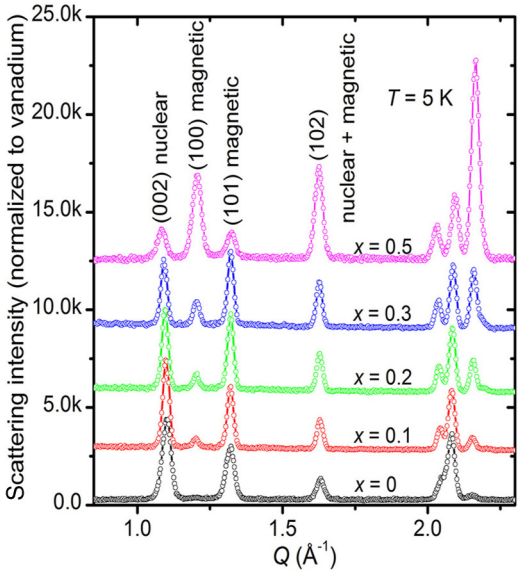

FIG. 4. The NPD patterns over a Q range of 0.8–2.3 $Å^{-1}$ for $LuMn_{1-x}Fe_xO_3$(x = 0,0.1,0.2,0.3, and 0.5) measured at 5 K. The patterns are shifted vertically for clarity. The data for $LuMn_{0.5}Fe_{0.5}O_3$ are taken from Ref. [2].

magnetic propagation vector is found to be $k = (0,0,0)$ for all samples. To fit the data, four 1D irreducible magnetic representations, $\Gamma_1(P6_3cm)$,$\Gamma_2(P6_3c'm')$,$\Gamma_3(P6_3'cm')$, and $\Gamma_4(P6_3'c'm)$, were generated by SARAh package. The calculated (100) nuclear reflection is so weak that the observed (100) reflection is considered to be of purely magnetic origin. Its intensity increases with increasing Fe doping. Because the magnetic (100) reflection is only allowed in the magnetic structure Γ_1 or Γ_3, the magnetic phases of the Fe-doped samples must contain contributions from Γ_1 or Γ_3 representation, whose percentage seems to increase with increasing Fe doping. Satisfying fit to the data for $LuMnO_3$ can be obtained by using either Γ_2 or Γ_4. The data for $LuMn_{1-x}Fe_xO_3$ (x = 0.1,0.2, and 0.3), on the other hand, cannot be fitted properly by any single 1D irreducible representation. The best fit requires a combination of irreducible representations, $(\Gamma_1 + \Gamma_2)$ or $(\Gamma_3 + \Gamma_4)$. The possible combinations, $(\Gamma_1 + \Gamma_4)$ or $(\Gamma_2 + \Gamma_3)$, are excluded because they result in unrealistic magnetic structures with different ordered moments at $z = 0$ and $1/2$ planes [33], and $(\Gamma_1 + \Gamma_2)$ and $(\Gamma_3 + \Gamma_4)$ are indistinguishable based only on the fit to NPD data. Nevertheless, first principle calculations may support the argument that $(\Gamma_3 + \Gamma_4)$ is a more favorable magnetic ground state for Mn-rich compounds of $LuMn_{1-x}Fe_xO_3$, given that the magnetic energies of Γ_3 and Γ_4 are much lower than those of Γ_1 and Γ_2 in $LuMnO_3$ [20,34,35]. This point has received strong experimental support from optical second harmonic spectroscopy [12] and neutron diffraction [19]. Moreover, an intermediate state between Γ_3 and Γ_4 can be stabilized due to their very close energies [20,24,34]. Therefore, we adopt the combination $(\Gamma_3 + \Gamma_4)$ as the magnetic ground state for the Fe-doped samples in this paper. The combined refinement of the crystal structure started with the XRD and NPD patterns measured at 300 K. The fitting results of the refinable parameters from this refinement were used as the starting values to refine the data for the next lower temperature. The successive refinements were also carried out in this way. Below T_N, magnetic phases were added to account for the magnetic contribution. All refinable structural parameters were kept the same after introducing magnetic phases. The refinements of crystallographic and magnetic phases were performed at the same time. We examined both $(\Gamma_1 + \Gamma_2)$ and $(\Gamma_3 + \Gamma_4)$ as the magnetic configuration in the refinement. They yielded equally good fitting results. There was no noticeable difference in the internal structural parameters when an alternate combination was used. Hereunder, we present the results of the refinement employing the combination $(\Gamma_3 + \Gamma_4)$, which is energetically more favorable as explained above. The summary of our Rietveld refinement results is given in Table I of the Supplemental Material [26].

Figure 5 shows the temperature dependence of the refined lattice constants, a and c, and the unit-cell volume V for $LuMn_{1-x}Fe_xO_3$ (x = 0,0.1,0.2, and 0.3). The a parameter decreases as temperature decreases from 300 to 30 K and remains nearly constant below 30 K. The thermal evolution of the unit-cell volume V is similar to that of the a parameter. The expansions of a and V from 5 to 300 K are ~0.015 Å and 1.7 $Å^3$ in all samples. When approaching T_N from below, the lattice constant c basically shows a negative thermal expansion, which becomes positive between 125 and 300 K. Similar thermal behavior of the lattice constant c of $LuMnO_3$ has also been observed in literature [5,36]. The length changes $\Delta c/c$ of the samples are all smaller than 0.04%. Considering the experimental resolution, we are unable to unambiguously correlate these changes with corresponding effects in the nuclear and/or magnetic structure. The change of c parameter reflects the interplay among the buckling and tilting of MnO_5 bipyramids and the variations of the Mn-O bond lengths. We attribute the minimum in the temperature dependence of c to a significant buckling of MnO_5 bipyramids, which is manifested by the reduction of O1-Mn/Fe-O2 angle when the temperature crosses T_N from below. It is clear that the thermal evolution in ab plane is more significant than in c direction. As the Fe-doping ratio increases from 0 to 0.3, the a parameter at base temperature decreases by about 0.02 Å, while the c parameter and the unit-cell volume increase by about 0.1 and 1.0 $Å^3$, respectively. The present evolution of a and c parameters with the Fe doping are in agreement with that reported for isostructural $YbMn_{1-x}Fe_xO_3$ [37].

The temperature dependence of the ordered magnetic moment, $m_{ord}(T)$, is plotted in Fig. 6(a). The ordered moments of the samples saturate between 3.2 and 3.5μ_B below 20 K and show no clear dependence on the Fe-doping ratio. Note that the maximum ordered spin-only moments of Mn^{3+} and Fe^{3+} are 4 and 5μ_B, respectively. The reduction of the ordered moments with respect to the spin-only values indicates that intrinsic magnetic fluctuation still exists in the ordered phase [8]. The $m_{ord}(T)$ of $LuMn_{0.8}Fe_{0.2}O_3$ within the temperature range between 50 and 100 K is fitted with a power law, $m_{ord}(T) \sim (1 - T/T_N)^{\beta}$. As shown by the dashed and dotted line in Fig. 6(a), the fit yields an ordering temperature of $T_N = 100.8 \pm 1.2$ K and $\beta = 0.21 \pm 0.03$. The value of β is smaller than that expected for a three-dimensional (3D) Heisenberg system, in agreement with the layered nature of the magnetic lattice in our samples.

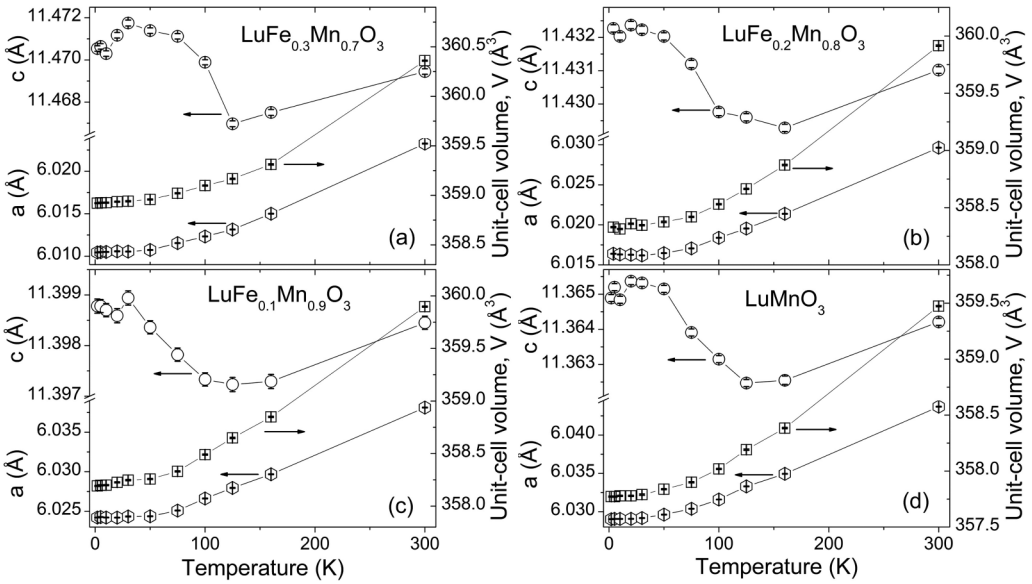

FIG. 5. Temperature dependence of the lattice constants, a and c, and the unit-cell volume for $LuMn_{1-x}Fe_xO_3$($x = 0,0.1,0.2$, and 0.3).

The x position of Mn ($x_$Mn) and the Mn-O bond distance are often considered as key parameters that describe the doping effect and determine the stability of the magnetic phases in h-RMnO$_3$ [17,18]. When $x\_\text{Mn} = 1/3$, the Mn ions form an ideal triangular lattice in the ab plane. The Mn-Mn exchange paths in the ab plane, as well as the interplane paths, are equivalent [18]. Deviation of $x_$Mn from 1/3 leads to different intraplane and interplane magnetic exchange interactions, which can be comprehended through the change in Mn-O bond distances. Such displacements of Mn atoms have a strong correlation with the magnetic structure and have been observed in various h-RMnO$_3$, e.g., $x\_\text{Mn} = 0.342$ for YMnO$_3$ [17] and 0.331 for LuMnO$_3$ [19] at 10 K. The temperature dependence of $x_$Mn/Fe in $LuMn_{1-x}Fe_xO_3$ is shown in Fig. 6(b). The data for $LuMn_{0.5}Fe_{0.5}O_3$ [2] is also shown for comparison. Below T_N, $x_$Mn/Fe of all samples is nearly constant and remains around the 1/3 threshold. Then, a sharp increase of $x_$Mn/Fe occurs at temperatures around T_N, suggesting strong spin-lattice coupling. In the case of LuMnO$_3$, $x_$Mn is 0.334 at 2 K and 0.344 at 300 K. The thermal evolution of $x_$Mn in our LuMnO$_3$ sample is a little different from that reported in literature [17]. Note that the samples with the same composition may have slight difference in structural properties due to the difference in synthesizing procedures [38,39].

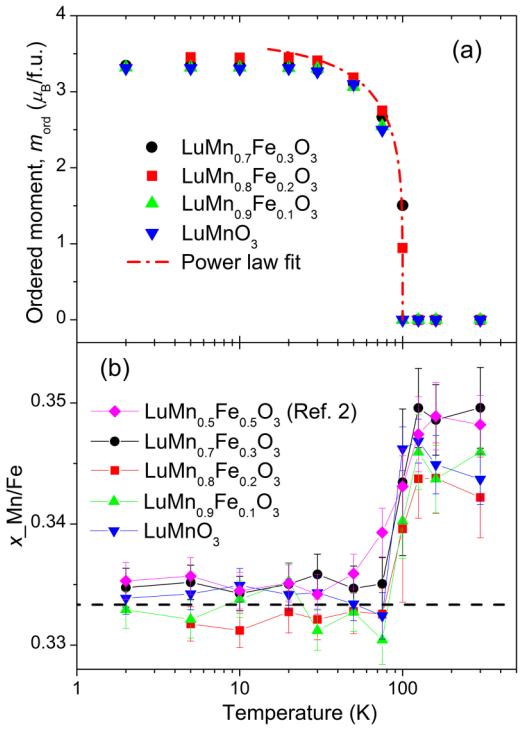

FIG. 6. (a) Temperature dependence of the ordered moments for $LuMn_{1-x}Fe_xO_3$($x = 0,0.1,0.2$, and 0.3). Dashed and dotted line represents a fit to the data for $LuMn_{0.8}Fe_{0.2}O_3$ with a power law. (b) Temperature dependence of the x position of Mn/Fe atoms, $x_$Mn/Fe, for $LuMn_{1-x}Fe_xO_3$($x = 0,0.1,0.2$, and 0.3).

The temperature dependence of the Mn/Fe-O bond distances are plotted in Figs. 7(a)–7(d). A schematic view of the oxygen coordination environment of Mn/Fe ions is given in the inset of Fig. 7(d). It is clear that both the apical and the basal Mn-O bond distances exhibit significantly change at T_N, reflecting the effect of atomic displacements as a result of the strong spin-lattice coupling. By mixing 1D irreducible representation Γ_3 and Γ_4, we obtain a 2D magnetic model with the space group $P6_3'$ as shown in Fig. 1(g). In this model, there is an angle (ψ) between the direction of the Mn/Fe moment at the position ($x_$Mn/Fe,0,0) and the a axis, i.e., $\psi = 0^\circ$ for Γ_3 and $\psi = 90^\circ$ for Γ_4. To investigate the evolution of ψ with temperature, we plot the temperature dependence of ψ for $LuMn_{1-x}Fe_xO_3$ ($x = 0.1,0.2,0.3$) in Fig. 7(e). Note that for all three samples, ψ increases with increasing temperature, corresponding to an overall rotation of the moments from Γ_3 to Γ_4. This is consistent with the recent first-principles calculations of the magnetic energies for LuMnO$_3$, which indicate that Γ_4 spin configuration is a little higher in energy

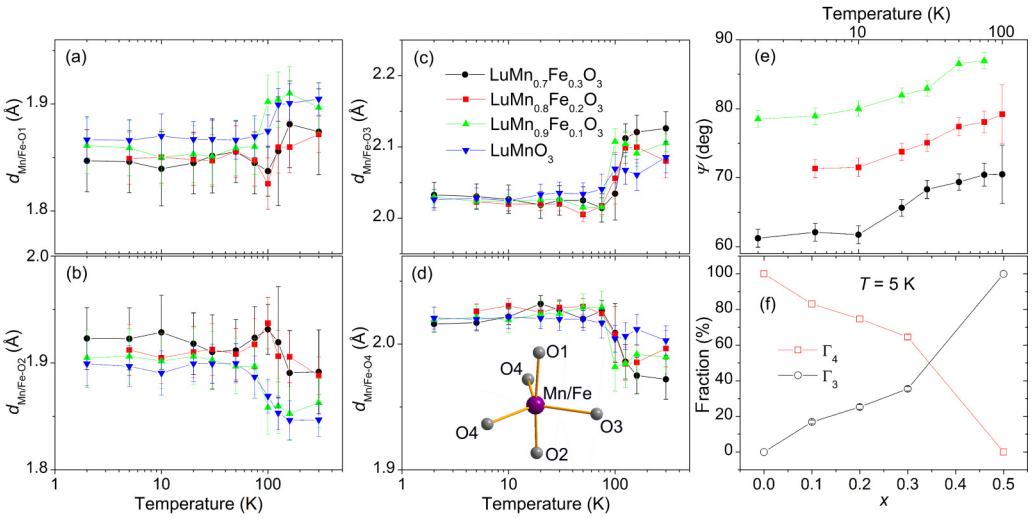

FIG. 7. Temperature dependence of the bond lengths, Mn/Fe-O1 (a), Mn/Fe-O2 (b), Mn/Fe-O3 (c), and Mn/Fe-O4 (d) for $LuMn_{1-x}Fe_xO_3$ (x = 0,0.1,0.2, and 0.3); the inset of (d) shows the oxygen coordination environment of Mn/Fe ions; (e) temperature evolution of the angle (ψ) between the direction of the Mn/Fe moment at the position (x_Mn/Fe,0,0) and the a axis in the Fe-doped samples; (f) the evaluated fractions of Γ_3 and Γ_4 as a function of the Fe concentration x.

than Γ_3 [34]. Figure 7(e) also suggests that ψ decreases with increasing Fe doping. This doping effect can be seen clearly in Fig. 7(f), where the percentages of Γ_3 and Γ_4 configurations are plotted as a function of Fe concentration. When the Fe-doping ratio increases from 0 to 0.5, the fraction of Γ_4 decreases from 100 to 0%. Therefore the observed change of magnetic structure upon Fe doping is interpreted as a chemically driven spin reorientation in the ab plane, while the spin reorientation with increasing temperature can be regarded as a thermally driven reorientation of the magnetic moments.

Besides the magnetic reflections below T_N, strong magnetic diffuse scattering has been revealed in our samples. The magnetic diffuse scattering has been widely observed in h-RMnO$_3$ and considered as the evidence of geometrical spin frustration in literature [7,19,32]. The representative NPD patterns at various temperatures for $LuMn_{0.7}Fe_{0.3}O_3$ are plotted in Fig. 8(a). The diffuse scattering of other samples shows similar temperature dependence with the one of $LuMn_{0.7}Fe_{0.3}O_3$. As seen in Fig. 8(a), clear magnetic diffuse scattering has emerged already at 160 K around the position of magnetic (100) reflection ($\sim$1.2 Å^{-1}) and is most pronounced at temperatures around T_N. As the spins start to order below T_N, this diffuse peak becomes subdued with further cooling from T_N. To extract the diffuse scattering, we subtracted off the background patterns, which were determined from the structure refinement of the diffraction patterns taken at the base temperature. Selected diffuse scattering patterns at temperatures close to T_N for $LuMn_{1-x}Fe_xO_3$ ($0 \leqslant x \leqslant 0.5$) are plotted as a function of Q in Figs. 8(b)–8(f). The NPD data for $LuMn_{0.5}Fe_{0.5}O_3$ is taken from Ref. [2]. A common feature about these diffuse peaks is the asymmetric shape (a fast rise at low Q and a slow fall towards high Q), which is characteristic of a 2D short-range order and agrees well with the profile of the weakly coupled Mn/Fe layers in $LuMn_{1-x}Fe_xO_3$. The magnetic diffuse scattering can then be described analytically by a modified Warren function for 2D magnetic correlations as follows [40–42],

$$P(Q)/{F_m}^2 = KmF_{hk}^2 \frac{1+(1-2(\lambda Q)^2/(4\pi)^2)^2}{2(\lambda Q/4\pi)^{3/2}} \times \left(\frac{\xi}{\lambda\sqrt{\pi}}\right)^{1/2} F(a) + C, \quad (1)$$

with

$$a = \xi(Q - Q_0)/(2\sqrt{\pi}), \quad (2)$$

and

$$F(a) = \int_0^{10} \exp[-(x^2 - a)^2]dx. \quad (3)$$

F_m is the magnetic form factor of magnetic ions, K is a scaling factor, m is the multiplicity of the 2D reflection (hk) with the magnetic structure factor F_{hk}, λ is the wavelength of neutrons, ξ is the 2D spin-spin correlation length, C is a scaling parameter of magnetic form factor, and Q_0 is the position of the reflection (hk). The fitting results are plotted in Figs. 8(b)–8(f). The 2D correlation length ξ, estimated from the above fitting, are summarized as a function of temperature in Fig. 8(g). The ξ for all samples decreases with increasing temperature. We do not see a regular pattern of the correlation length upon Fe doping, which could be hindered by the large error bars due to the noisy diffuse signal obtained by subtraction. Polarized neutron scattering technique will be necessary to characterize the correlation lengths more precisely [43–45]. The fit with the Warren function shows that the diffuse scattering is most likely due to the short-range order that originates from the strong exchange coupling in the ab planes. At T_N, the 3D magnetic order occurs when the ab planes are locked in with respect to each other due to the interplane exchange interactions [46]. Our analysis suggests that the low dimensionality of the magnet lattice plays a more important

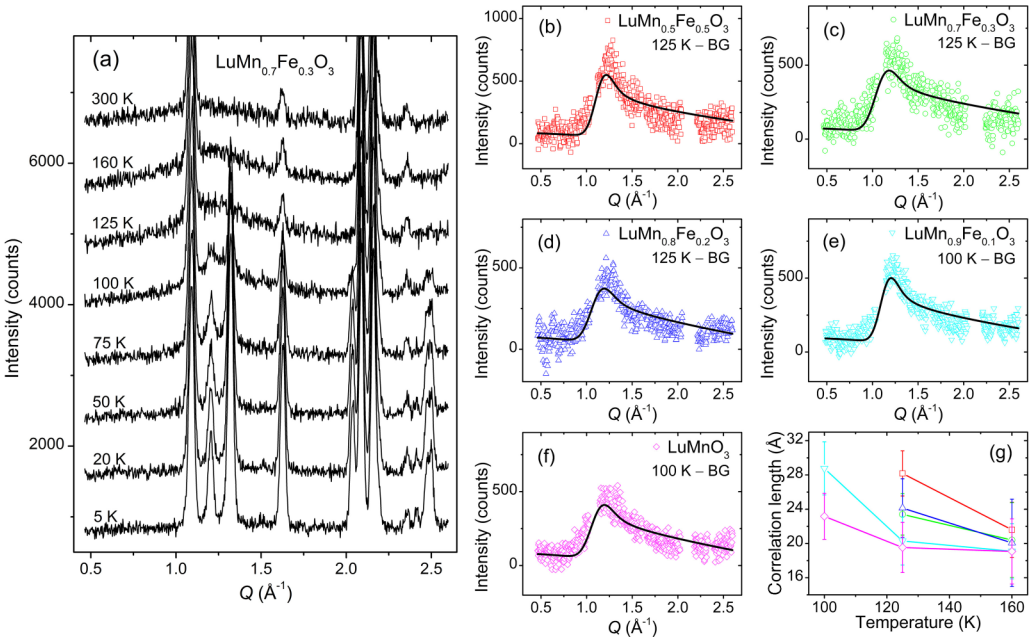

FIG. 8. (a) Selected NPD patterns for $LuMn_{0.7}Fe_{0.3}O_3$ at various temperatures; (b)–(f) magnetic diffuse scattering for $LuMn_{1-x}Fe_xO_3 (0 \leqslant x \leqslant 0.5)$ obtained by subtracting the background pattern determined with the Rietveld refinement. The black lines are the fit with 2D Warren function; (g) the temperature dependence of the 2D correlation lengths for $LuMn_{1-x}Fe_xO_3 (0 \leqslant x \leqslant 0.5)$.

role than the geometrical frustration in shaping the magnetic behaviors of $LuMn_{1-x}Fe_xO_3$.

IV. DISCUSSION

Our structural characterization confirms that the $P6_3cm$ hexagonal symmetry, common in the h-RMnO$_3$ family, is preserved in $LuMn_{1-x}Fe_xO_3$ ($0 \leqslant x \leqslant 0.3$), within the temperature range of 2–300 K. Strong magnetoelastic coupling occurs in the studied samples through the large atomic displacements around T_N. With increasing Fe doping, we observed an increase of the lattice constant c and the unit-cell volume but a small decrease of the lattice constant a. The change of c is stronger than the change of a upon Fe doping, suggesting that the equivalent chemical pressure introduced by Fe doping is stronger in c axis than in the basal plane. On the contrary, Y doping to the Lu site causes stronger chemical pressure effect in the basal plane [19]. The expansion of c with Fe doping mainly reflects the increased buckling of Mn/Fe-O_5 polyhedra [15]. Applying either chemical or physical pressure may produce a subtle change in the magnetic easy axis and, in turn, a spin reorientation in $YMnO_3$ [19,47]. Although no change in the symmetry of the triangular AFM state of $LuMnO_3$ was observed at a high pressure of 6 GPa [21], spin reorientation in the ab plane may occur by either Y [19] or Fe (this paper) doping in $LuMnO_3$. We have found that the rotation angle ψ decreases from 90 to 0° as the Fe-doping ratio increases from 0 to 0.5. We also notice in a recent paper [24] on Mn-doped h-$LuFeO_3$ that the ground-state spin configuration shows a rotation from Γ_2 to Γ_1 (or Γ_3) via an intermediate representation ($\Gamma_2 + \Gamma_1/\Gamma_3$) as the Mn concentration increases from 0.25 to 0.5. These results highlight the composition-driven spin reorientation owing to the chemical disturbance to the single phase compound.

We observed a small peak at 55 K in the temperature-dependent magnetization of $LuMn_{0.7}Fe_{0.3}O_3$ in Fig. 2(a). Such a peak also exists in $LuMn_{0.5}Fe_{0.5}O_3$ [2,24]. We attribute this peak to a spin-reorientation behavior, similar to the ones found in $LuFe_{1-x}Mn_xO_3$ ($x = 0.25$ and 0.33) [24], $LuFeO_3$ [48], $HoMnO_3$ [49], and $ScMnO_3$ [50]. As argued in Ref. [18], the spin-reorientation transition at T_{SR} in h-RMnO$_3$ family correlates strongly with the Mn position, i.e., the spin reorientation happens when x_Mn crosses the 1/3 threshold. However, in both $LuMn_{0.7}Fe_{0.3}O_3$ and $LuMn_{0.5}Fe_{0.5}O_3$, no such cross has been observed around T_{SR} within the resolution of our NPD experiments [see Fig. 6(b)]. In contrast to the NPD data of $LuFe_{1-x}Mn_xO_3$ ($x = 0.25$ and 0.33) [24], those of $LuMn_{0.7}Fe_{0.3}O_3$ show no noteworthy change across $T_{SR} = 55$ K, as shown in Fig. 8(a). It is suggested in Fig. 7(e) that this spin reorientation is a gradual spin rotation taking place between the base temperature and T_N. Although the spin reorientation appears as a peak in magnetization only for $LuMn_{0.7}Fe_{0.3}O_3$, as seen in Fig. 2(a), this thermally driven spin reorientation should also exist in $LuMn_{0.8}Fe_{0.2}O_3$ and $LuMn_{0.9}Fe_{0.1}O_3$. There is seemingly a very broad hump in the temperature dependence of magnetization of $LuMn_{0.8}Fe_{0.2}O_3$ and $LuMn_{0.9}Fe_{0.1}O_3$ at around 55 K, as compared with the curve of $LuMnO_3$. Therefore, the spin reorientation at T_{SR} can also be taken as evidence of the drastic effect due to Fe doping. A precise determination of the nature of the spin reorientation in these compounds requires detailed neutron investigations on single crystals.

A relatively complete understanding to the $LuMn_{1-x}Fe_xO_3$ series is achieved by combining the results of this paper and Ref. [24], as summarized in the magnetic phase diagram in Fig. 9 as functions of temperature and the Fe concentration. The T_N of h-$LuFeO_3$ and $LuMn_{0.5}Fe_{0.5}O_3$ are taken from Refs. [51,2], respectively. The magnetic phase of

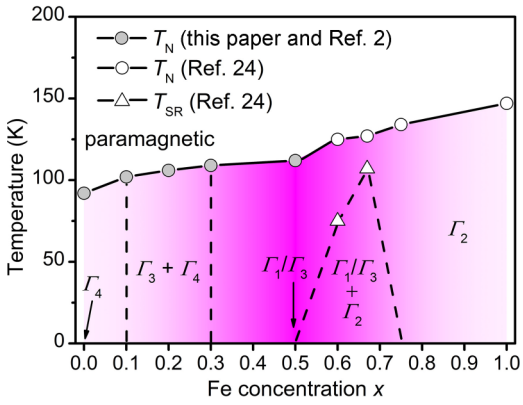

FIG. 9. Magnetic phase diagram determined from neutron scattering measurements. The diagram for $x > 0.5$ is taken from Ref. [24]. The T_N and spin representation for $x = 0.5$ are taken from Ref. [2].

$LuMn_{1-x}Fe_xO_3$ for $0.3 < x < 0.5$ and $0 < x < 0.1$ below T_N is still unclear, but it is reasonable to presume that mixed spin presentations emerge as well in the magnetic ground states of these compositions. It is obvious that T_N increases almost linearly with increasing Fe concentration. The magnetic transition temperature of h-$LuMnO_3$ is thus tunable by tailoring the transition-metal composition.

V. CONCLUSION

We have studied the nuclear and magnetic structures of $LuMn_{1-x}Fe_xO_3$ ($x = 0,0.1,0.2$, and 0.3) using magnetic measurements and neutron/x-ray powder diffraction. The nuclear structures of the samples preserve the $P6_3cm$ space group of h-$RMnO_3$. The atomic positions undergo clear displacements at T_N, suggesting strong spin-lattice coupling. The magnetic ground state has been evaluated with a mixed spin configuration of Γ_3 and Γ_4 representations for the Fe-doped samples and a single representation of Γ_4 for $LuMnO_3$. The short-range order has been evidenced by the diffuse neutron scattering and attributed to the strong exchange couplings in ab planes. A composition-driven spin reorientation introduced by Fe doping has been highlighted. A thermally driven spin rotation from Γ_3 to Γ_4 has also been revealed in the Fe-doped samples, as the temperature changes from the base temperature to T_N. It is confirmed that the AFM transition temperature of h-$LuMnO_3$ can be raised by Fe doping.

ACKNOWLEDGMENT

We thank Dr. Kirill Nemkovski for his help in neutron scattering experiments. The work was partially performed at SINQ, PSI, Switzerland.

[1] R. D. Johnson and P. G. Radaelli, Annu. Rev. Mater. Res. **44**, 269 (2014) and references therein.
[2] H. S. Nair, Z. Fu, C. M. N. Kumar, V. Y. Pomjakushin, Y. Xiao, T. Chatterji, and A. M. Strydom, Europhys. Lett. **110**, 37007 (2015).
[3] T. Katsufuji, M. Masaki, A. Machida, M. Moritomo, K. Kato, E. Nishibori, M. Takata, M. Sakata, K. Ohoyama, K. Kitazawa, and H. Takagi, Phys. Rev. B **66**, 134434 (2002).
[4] F. Yen, C. R. dela Cruz, B. Lorenz, Y. Y. Sun, Y. Q. Wang, M. M. Gospodinov, and C. W. Chu, Phys. Rev. B **71**, 180407 (R) (2005).
[5] S. Lee, A. Pirogov, J. H. Han, J.-G. Park, A. Hoshikawa, and T. Kamiyama, Phys. Rev. B **71**, 180413(R) (2005).
[6] H. L. Yakel, W. C. Koehler, E. F. Bertaut, and E. F. Forrat, Acta Crystallogr. **16**, 957 (1963).
[7] P. A. Sharma, J. S. Ahn, N. Hur, S. Park, S. B. Kim, S. Lee, J.-G. Park, S. Guha, and S.-W. Cheong, Phys. Rev. Lett. **93**, 177202 (2004).
[8] T. J. Sato, S.-H. Lee, T. Katsufuji, M. Masaki, S. Park, J. R. D. Copley, and H. Takagi, Phys. Rev. B **68**, 014432 (2003).
[9] A. Muñoz, J. A. Alonso, M. J. Martínez-Lope, M. T. Casáis, J. L. Martínez, and M. T. Fernández-Díaz, Phys. Rev. B **62**, 9498 (2000).
[10] E. F. Bertaut and M. Mercier, Phys. Lett. A **5**, 27 (1964).
[11] J. Park, U. Kong, A. Pirogov, S. I. Choi1, J.-G. Park, Y. N. Choi, C. Lee, and W. Jo, Appl. Phys. A **74**, S796 (2002).
[12] M. Fiebig, D. Fröhlich, K. Kohn, St. Leute, Th. Lottermoser, V. V. Pavlov, and R. V. Pisarev, Phys. Rev. Lett. **84**, 5620 (2000).
[13] D. Fröhlich, St. Leute, V. V. Pavlov, and R. V. Pisarev, Phys. Rev. Lett. **81**, 3239 (1998).
[14] M. C. Sekhar, S. Lee, G. Choi, C. Lee, and J.-G. Park, Phys. Rev. B **72**, 014402 (2005).
[15] S. Namdeo, S. S. Rao, S. D. Kaushik, V. Siruguri, and A. M. Awasthi, J. Appl. Phys. **116**, 024105 (2014).
[16] P. J. Brown and T. Chatterji, J. Phys.: Condens. Matter **18**, 10085 (2006).
[17] S. Lee, A. Pirogov, M. Kang, K.-H. Jang, M. Yonemura, T. Kamiyama, S.-W. Cheong, F. Gozzo, N. Shin, H. Kimura, Y. Noda, and J.-G. Park, Nature (London) **451**, 805 (2008).
[18] X. Fabrèges, S. Petit, I. Mirebeau, S. Pailhès, L. Pinsard, A. Forget, M. T. Fernandez-Diaz, and F. Porcher, Phys. Rev. Lett. **103**, 067204 (2009).
[19] J. Park, S. Lee, M. Kang, K.-H. Jang, C. Lee, S. V. Streltsov, V. V. Mazurenko, M. V. Valentyuk, J. E. Medvedeva, T. Kamiyama, and J.-G. Park, Phys. Rev. B **82**, 054428 (2010).
[20] I. V. Solovyev, M. V. Valentyuk, and V. V. Mazurenko, Phys. Rev. B **86**, 054407 (2012).
[21] D. P. Kozlenko, S. E. Kichanov, S. Lee, J.-G. Park, V. P. Glazkov, and B. N. Savenko, JETP Lett. **83**, 346 (2006).
[22] S. L. Samal, W. Green, S. E. Lofland, K. V. Ramanujachary, D. Das, and A. K. Ganguli, J. Solid State Chem. **181**, 61 (2008).
[23] N. Sharma, A. Das, C. L. Prajapat, and S. S. Meena, J. Magn. Magn. Mater. **348**, 120 (2013).
[24] S. M. Disseler, X. Luo, B. Gao, Y. S. Oh, R. Hu, Y. Wang, D. Quintana, A. Zhang, Q. Huang, J. Lau, R. Paul, J. W. Lynn, S.-W. Cheong, and W. Ratcliff II, Phys. Rev. B **92**, 054435 (2015).
[25] T. Katsufuji, S. Mori, M. Masaki, Y. Moritomo, N. Yamamoto, and H. Takagi, Phys. Rev. B **64**, 104419 (2001).
[26] See Supplemental Material at http://link.aps.org/supplemental/10.1103/PhysRevB.94.125150 for the temperature-dependent XRD patterns and the detailed Rietveld refinement results.

[27] P. Fischer, G. Frey, M. Koch, M. Könnecke, V. Pomjakushin, J. Schefer, R. Thut, N. Schlumpf, R. Bürge, U. Greuter, S. Bondt, and E. Berruyer, Physica B **276**, 146 (2000).
[28] M. Hoelzel, A. Senyshyn, and O. Dolotko, J. Large-Scale Res. Facil. **1**, A5 (2015).
[29] A. S. Wills, Physica B **276**, 680 (2000).
[30] H. M. Rietveld, J. Appl. Crystallogr. **2**, 65 (1969).
[31] J. Rodriguez-Carvajal, Physica B **192**, 55 (1993).
[32] J. Park, J.-G. Park, G. S. Jeon, H.-Y. Choi, C. Lee, W. Jo, R. Bewley, K. A. McEwen, and T. G. Perring, Phys. Rev. B **68**, 104426 (2003).
[33] J. Park, M. Kang, J. Kim, S. Lee, K.-H. Jang, A. Pirogov, J.-G. Park, C. Lee, S.-H. Park, and H. C. Kim, Phys. Rev. B **79**, 064417 (2009).
[34] H. Das, A. L. Wysocki, Y. Geng, W. Wu, and C. J. Fennie, Nat. Commun. **5**, 2998 (2014).
[35] H. Tan, C. Xu, M. Li, S. Wang, B.-L. Gu, and W. Duan, J. Phys.: Condens. Matter **28**, 126002 (2016).
[36] B. B. Van Aken and T. T. M. Palstra, Phys. Rev. B **69**, 134113 (2004).
[37] Y.-H. Huang, M. Karppinen, N. Imamura, H. Yamauchi, and J. B. Goodenough, Phys. Rev. B **76**, 174405 (2007).
[38] P. Tong, D. Louca, N. Lee, and S.-W. Cheong, Phys. Rev. B **86**, 094419 (2012).
[39] B. B. Van Aken, A. Meetsma and T. T. M. Palstra, Acta Crystallogr. Sec. E **57**, i101 (2001).
[40] L. L. Lumata, T. Besara, P. L. Kuhns, A. P. Reyes, H. D. Zhou, C. R. Wiebe, L. Balicas, Y. J. Jo, J. S. Brooks, Y. Takano, M. J. Case, Y. Qiu, J. R. D. Copley, J. S. Gardner, K. Y. Choi, N. S. Dalal, and M. J. R. Hoch, Phys. Rev. B **81**, 224416 (2010).
[41] A. S. Wills, N. P. Raju, C. Morin, and J. E. Greedan, Chem. Mater. **11**, 1936 (1999).
[42] B. E. Warren, Phys. Rev. **59**, 693 (1941).
[43] Z. Fu, Y. Zheng, Y. Xiao, S. Bedanta, A. Senyshyn, G. G. Simeoni, Y. Su, U. Rücker, P. Kögerler, and T. Brückel, Phys. Rev. B **87**, 214406 (2013).
[44] Z.-D. Fu, P. Kögerler, U. Rücker, Y. Su, R. Mittal, and T. Brückel, New J. Phys. **12**, 083044 (2010).
[45] H. S. Nair, Z. Fu, J. Voigt, Y. Su, and T. Brückel, Phys. Rev. B **89**, 174431 (2014).
[46] Th. Brückel, C. Paulsen, W. Prandl, and L. Weiss, J. Phys. I France **3**, 1839 (1993).
[47] D. P. Kozlenko, S. E. Kichanov, S. Lee, J.-G. Park, V. P. Glazkov, and B. N. Savenko, JETP Lett. **82**, 193 (2005).
[48] H. Wang, I. V. Solovyev, W. Wang, X. Wang, P. J. Ryan, D. J. Keavney, J.-W. Kim, T. Z. Ward, L. Zhu, J. Shen, X. M Cheng, L. He, X. Xu, and X. Wu, Phys. Rev. B **90**, 014436 (2014).
[49] B. Lorenz, A. P. Litvinchuk, M. M. Gospodinov, and C. W. Chu, Phys. Rev. Lett. **92**, 087204 (2004).
[50] M. Bieringer and J. E. Greedan, J. Solid State Chem. **143**, 132 (1999).
[51] J. A. Moyer, R. Misra, J. A. Mundy, C. M. Brooks, J. T. Heron, D. A. Muller, D. G. Schlom, and P. Schiffer, APL Mater. **2**, 012106 (2014).